

Fault Geometry and the Dynamics of the 1999 Chi-Chi (Taiwan) Earthquake

by David D. Oglesby* and Steven M. Day

Abstract The 1999 M 7.6 Chi-Chi (Taiwan) earthquake produced a data set of unparalleled size and quality, particularly in the near-source region where data have been previously quite scarce. The large amount of near-source data allows the verification of many predictions of thrust-fault behavior for faults that intersect the surface of the earth. Through rigorous three-dimensional dynamic models of the Chi-Chi earthquake, it can be shown that many aspects of the observed near-source ground motion in this event are direct effects of the asymmetrical dipping fault geometry. These effects include the hanging wall moving more than the footwall (with strongly peaked velocities right at the fault trace) and a transition from predominantly thrust motion in the south of the fault to largely left-lateral motion in the north. Building on the work of Oglesby and Day (2001), the current work helps to delineate the effects of fault geometry, nonuniform prestress, and dynamic waves on the physics of the Chi-Chi earthquake and dip-slip faults in general. In particular, we find that a completely homogeneous prestress pattern still fits the gross features of the near-source ground motion quite well. Additionally, the strike-slip component of motion near the fault trace is seen to be a combination of dynamic and static effects. Finally, dynamic overshoot is seen to be much larger for dip-slip faults than for otherwise identical vertical faults. The results emphasize the necessity of rigorous models that correctly account for both the effects of fault geometry and dynamic waves in the rupture and slip processes.

Introduction

The M 7.6 1999 Chi-Chi (Taiwan) earthquake will undoubtedly be recognized as one of the most significant earthquakes for the science of seismology, due to the unprecedented amount of high-quality near-source data that it generated (Lee *et al.*, 1999). This wealth of data not only allows more precise determination of faulting models of this event, but also addresses new questions concerning faulting and dynamics. In particular, this event allows the verification of many predictions of ground-motion behavior in the near-source area of dip-slip faults, where data have been especially scarce to date. In this article, we show that many of the observations of the near-source displacements and peak velocities can be explained as simple consequences of the asymmetric, dipping fault geometry, with no assumptions of stress inhomogeneity, complicated friction laws, or site/path effects. These observations include the hanging wall moving much more than the footwall, with both a strong discontinuity and a strong peak at the fault trace; a transition from thrust-directed motion in the south to left-lateral strike-slip

motion in the north, and a possible mismatch between near-field and far-field estimates of faulting style and energy. Oglesby and Day (2001) performed an initial examination of the effect of the dipping fault geometry on the Chi-Chi earthquake, showing that a simple (yet rigorous) dynamic model, which includes the effect of the dipping fault geometry, can explain some key features of the recorded low-frequency ground motion. The present work uses a more extensive set of numerical simulations to further examine the influence of the dipping fault geometry on this earthquake and explores in much more detail the consequences of the results. In the present work we (1) separate the effects of stress heterogeneity from the effects of fault geometry, and (2) examine effects of inertial dynamics (versus elastostatics) in controlling the fault slip and ground displacement patterns.

The Chi-Chi earthquake (Fig. 1) took place on a largely north–south–trending fault in Western Taiwan, identified at the surface exposure as the Chelungpu fault, with a length along strike of approximately 80 km (Chin *et al.*, 2000). Even though the U.S. Geological Survey moment tensor shows a thrust-oriented rake of 67° for this event, surface measurements of slip along the fault trace show a significant

*Present address: Department of Earth Sciences, University of California, Riverside, Riverside, California, 92521; david.oglesby@ucr.edu.

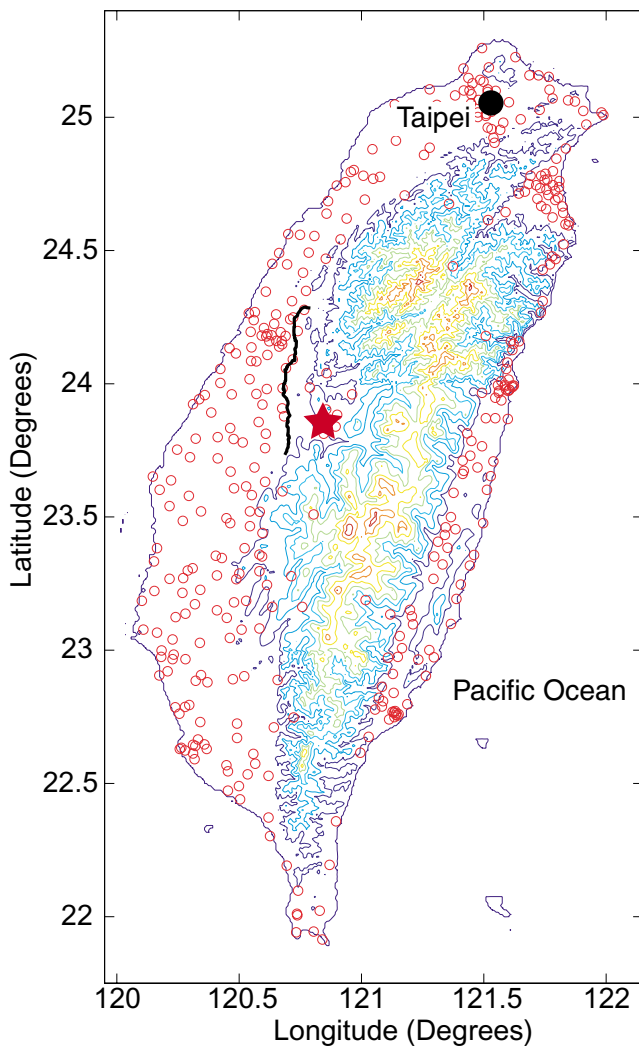


Figure 1. Map of Taiwan showing the 1999 Chi-Chi fault trace (black), the network of seismic stations (red circles), and the epicenter of the Chi-Chi event (red star).

left-lateral component in the northern portions of the fault (Shin *et al.*, 2001). This spatial transition from thrust to left-lateral motion is also observed in the strong-motion data (Lee *et al.*, 1999) and the Global Positioning System (GPS) measurements (Rau *et al.*, 1999, Zeng and Chen, 2001). Because of the wealth of data, there has been much work performed on the kinematics and dynamics of this earthquake. Teng (2000), based on multiple phases in the near-source data, has argued that the rupture front is discontinuous, with multiple episodes of fault slip on different parts of the fault. Noting that acceleration and damage was concentrated in the south but that displacements were much higher in the north, Mori and Ma (2000) and Song (2000) have argued that the frictional properties of the fault were strongly inhomogeneous, leading to a higher ratio of displacement to acceleration in the north than in the south. These models emphasize

how much can be learned about the physics of the faulting process when copious near-source data are available. In contrast to most of these previous studies, which examine the fine structure of rupture propagation and slip on the fault, the current work attempts to isolate purely geometrical effects on a larger, more coarse scale.

The effects of fault geometry on the dynamics of the earthquake process have been explored in many recent articles. For example, Harris *et al.* (1991), Harris and Day (1993), Harris and Day (1999), Kase and Kuge (1998), and Magistrale and Day (1999) have simulated the dynamics of faults with parallel and orthogonal segments and offsets. They found that the ability of an earthquake rupture to jump a fault offset is related to both the relative positions of the fault segments and the stress distribution on the fault. Closer to the subject of the Chi-Chi earthquake, it has been previously argued that the dynamics of dip-slip faults (especially those that intersect the free surface of the earth) are strongly affected by their fault geometry (Mikumo and Miyatake, 1993; Rudniki and Wu, 1995; Brune, 1996; Nielsen, 1998; Oglesby *et al.*, 1998; Shi *et al.*, 1998, Bonafede and Neri, 2000; Oglesby *et al.*, 2000a,b). In particular, these studies showed that in comparison with vertical strike-slip faults, dip-slip faults exhibit many unique features associated with their asymmetrical geometry. These effects include reflections from the free surface that cause a feedback between the rupture and radiation processes, leading to thrust faults having greater dynamic stress drops, greater fault motion, and greater near-source ground motion than normal faults. Also, the smaller size of the hanging wall (coupled with the possibility of trapped waves between the fault and the free surface) leads to an asymmetry between hanging-wall and footwall motion that can be a factor of 4 or more near the free surface. Additionally, at the up-dip corners of the fault there can be a large temporal and spatial rotation of rake, leading to a strong strike-slip component of motion near the edges of the fault trace. It should be emphasized that all these effects are strongly dependent on the fault either intersecting or closely approaching the free surface, and that most of these predictions are for the near-source (less than 10 km from the fault trace) area. Because of the lack of near-source strong-motion or GPS data for previous earthquakes of this type (e.g., the 1971 San Fernando, California, earthquake), evidence for these effects has been largely based on qualitative (although highly suggestive) measures (e.g., Allen *et al.*, 1998). However, the 1999 Chi-Chi earthquake provides a unique opportunity to determine if these features are found in actual earthquakes and to determine how important they are in comparison to other factors, such as the frictional and stress characteristics on the fault. This final point is especially important, because fault geometry, unlike the friction and stress properties on the fault, can (at least in principle) be determined in advance. Thus, we are given the tantalizing hope of predicting some of the gross features of ground motion in advance.

Method

To implement the nonorthogonal model geometry, we use the three-dimensional, explicit finite-element method (Whirley and Engelman, 1993; Oglesby, 1999). Our model geometry is the same as in Oglesby and Day (2001), with physical and computational parameters shown in Table 1. To separate the geometrical effects from the effects of three-dimensional material structure, we place our fault in a homogeneous half-space. This assumption leads to an underprediction of displacements and velocities in our model, but it is required to isolate the effects of fault geometry from the effects of earth structure. To further isolate the purely geometrical effects on the faulting process, we start with a completely homogeneous (amplitude and direction) stress distribution. In this case, the normal stress should be thought of as an effective normal stress, taking into account pore pressure or other effects that would lead to an approximately depth-independent stress drop. Our final, preferred result (from Oglesby and Day, 2001) uses a slightly inhomogeneous stress distribution, with a high-stress circular (radius 16 km) asperity in the northern part of the fault, centered at 22 km down-dip, and 25 km along strike from the northern end. The center of this asperity has peak shear and normal stresses of 10 times the ambient level on the fault. The stresses taper linearly to the ambient level of stress at a radius of 10 km. The direction of the shear prestress throughout the fault is still constant and is the same as in the homogeneous case (i.e., the resolved shear prestress on the fault plane is set to a rake angle of 67°). The asperity was added to better match the high displacements in the northern part of the near-source region, but the specific parameters such as its size and location are not well constrained by our analysis. However, as will be pointed out in the results, the main features of the low-frequency ground motion do not require this asperity and are rather insensitive to its position and size.

We use a simple slip-weakening (Ida, 1972; Andrews, 1976; Day, 1982) Coulomb friction law of $\tau_{\text{friction}} = \mu\sigma_{\text{normal}}$, with a coefficient of friction μ that varies linearly with cumulative fault slip. It should be emphasized that our goal is to reproduce the spatial pattern of ground motion (due to geometrical effects) in the Chi-Chi earthquake, not to perform a complete waveform match between the data and our synthetic ground motions. However, the methods used in this study can provide a valuable starting point for more detailed dynamic waveform models in the future. In addition, the results show that a successful dynamic model of this event needs to account for the dipping fault geometry and the effects of the free surface on rupture and slip.

For comparison with recorded velocities and displacements, we integrated the digital accelerograms compiled by Lee *et al.* (1999) using the method of Oglesby and Day (2001). Prior to the first integration of each record, we removed the pre-event mean from the accelerogram. Prior to the second integration, we made another baseline correction, requiring both the slope and mean of the velocity record to

Table 1

Physical and Computational Parameters

Density	3000 kg/m ³
Shear modulus	3×10^{10} Pa
Poisson ratio	0.25
Initial shear stress (homogeneous model)	3.2×10^6 Pa
Initial normal stress (homogeneous model)	6×10^6 Pa
Initial background shear stress (asperity model)	1.6×10^6 Pa
Initial background normal stress (asperity model)	3×10^6 Pa
Rake angle (direction) of shear stress	67°
Static frictional coefficient	0.7
Sliding frictional coefficient	0.3
Critical slip-weakening distance	5 cm
Element size on fault	500 m \times 500 m
Maximum calculated frequency	0.6 Hz

be 0 following the cessation of the strongest shaking (as measured by the 90th quantile of the cumulative squared velocity), an approach similar to that of Iwan (1985). The second integration can be highly sensitive to the choice of the time window over which the velocity mean and slope corrections are estimated (e.g., Boore, 1999). In general, this choice can be quite subjective. However, the key records considered here are large in amplitude and recorded close to the fault trace, with the result that the dominant ground motion is relatively pulselike. Under these circumstances, there is relatively little ambiguity in the time of termination of the motion, and the velocity baseline correction (mean and slope) and integration to displacement can likewise be made with little ambiguity. To further minimize uncertainties in peak displacement associated with uncertainties in the second baseline correction, we use for our analysis the peak motion over the first 40 sec of total record time (which includes about 20 sec of pre-event recording). In addition to greatly reducing the sensitivity to baseline uncertainties, this time windowing corresponds well with the duration of the simulations and it excludes late-arriving energy, which is probably attributable to unmodeled scatterers. Because the simulation results are band limited to approximately 0.6 Hz, to provide a valid comparison both the data and the simulated velocities were low-pass filtered using a first-order Butterworth filter with a corner frequency of 0.6 Hz.

Results

Integration of Acceleration Data

While this article was under review, GPS data for the Chi-Chi earthquake became widely available from the Institute of Earth Science, Academia Sinica (Zeng and Chen, 2001). As a check of the acceleration integration methodology described previously, in Figure 2a we compare the integrated acceleration data with the GPS data. Overall the patterns from the two data sets are quite similar, displaying greater displacement on the hanging wall than on the footwall, a rotation of slip direction from thrust-oriented in the south to oblique left-lateral in the north, and higher displace-

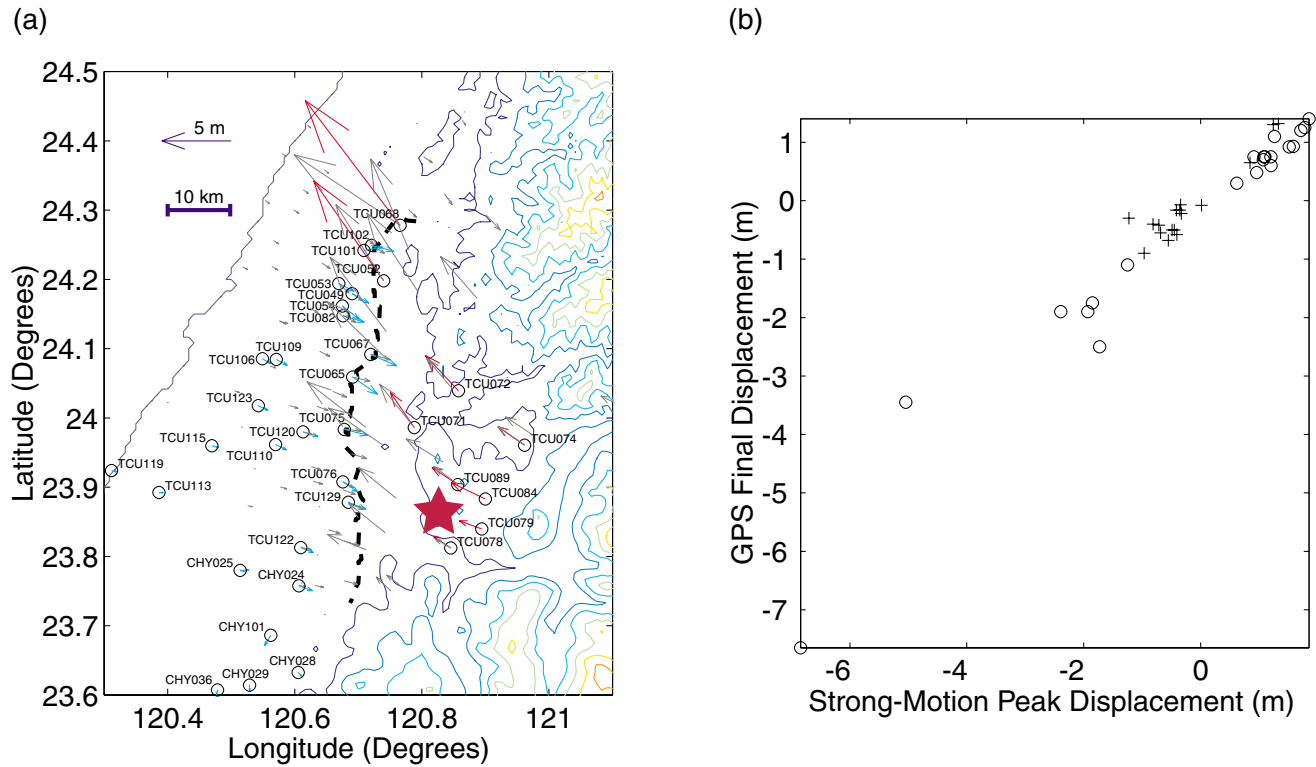


Figure 2. (a) Comparison of peak integrated strong-motion displacement (red and blue arrows) and final GPS displacement (gray arrows). With the exception of station TCU068, the correspondence is quite good. (b) Scatter plot of final GPS displacement versus peak integrated strong-motion displacement. Circles represent the east component, and pluses represent the north component.

ments in the north. At collocated GPS and strong-motion stations we may directly compare the amplitudes and directions of each measured displacement. A quantitative analysis results in a correlation coefficient of 0.98 between the east–west components of GPS and strong-motion displacement and a correlation coefficient of 0.97 between the north–south components. However, the integrated peak displacements are systematically slightly higher than the GPS displacements: A linear fit to a plot of north–south GPS final displacements versus east–west strong-motion peak displacements (Fig. 2b) gives a line with slope 0.67 and an intercept of 0.11 m. A similar fit to the east–west components gives a slope of 0.90 and an intercept of -0.26 m. Because typical displacement time histories display a peak and then a decay to the final value, it is expected that the peak strong-motion displacements should be larger than the final GPS displacements. In our subsequent results, we compare peak displacements in our dynamic models to peak displacements in the strong-motion data, so our model comparisons are not biased by this effect. Furthermore, the present work focuses on the spatial pattern of ground motion, so the absolute amplitude of ground motion is less important in our analysis. An additional bias in the match between the strong-motion and GPS data is caused by the anomalous direction of the GPS displacement at station TCU068, which has a much smaller

north component than the corresponding strong-motion peak displacement. With this station removed from the analysis, the fit improves and becomes consistent between the two components of motion. The slope and intercept of the best-fitting line to the north–south components become 0.81 and 0.11 m, respectively, and the corresponding values for the east–west components become 0.77 and -0.18 m. The net result of this comparison is to confirm that the integrated strong-motion data give a correct representation of the near-field displacement. There are no large errors in the strong-motion data processing, and the areas where strong-motion data are missing (in particular, the southern part of the hanging wall near the fault trace) do not display a ground-motion pattern substantially different from areas where strong-motion coverage is greater.

Homogeneous Prestress Model

The final fault plane displacements resulting from completely homogeneous shear and normal prestress distributions on the fault are shown in Figure 3. One obvious feature of the model is the asymmetry between hanging wall (on the right of the figure) and footwall (on the left) displacement. The near-surface region of the hanging wall has a much higher (by a factor of approximately 3) displacement than the corresponding region of the footwall. This effect is en-

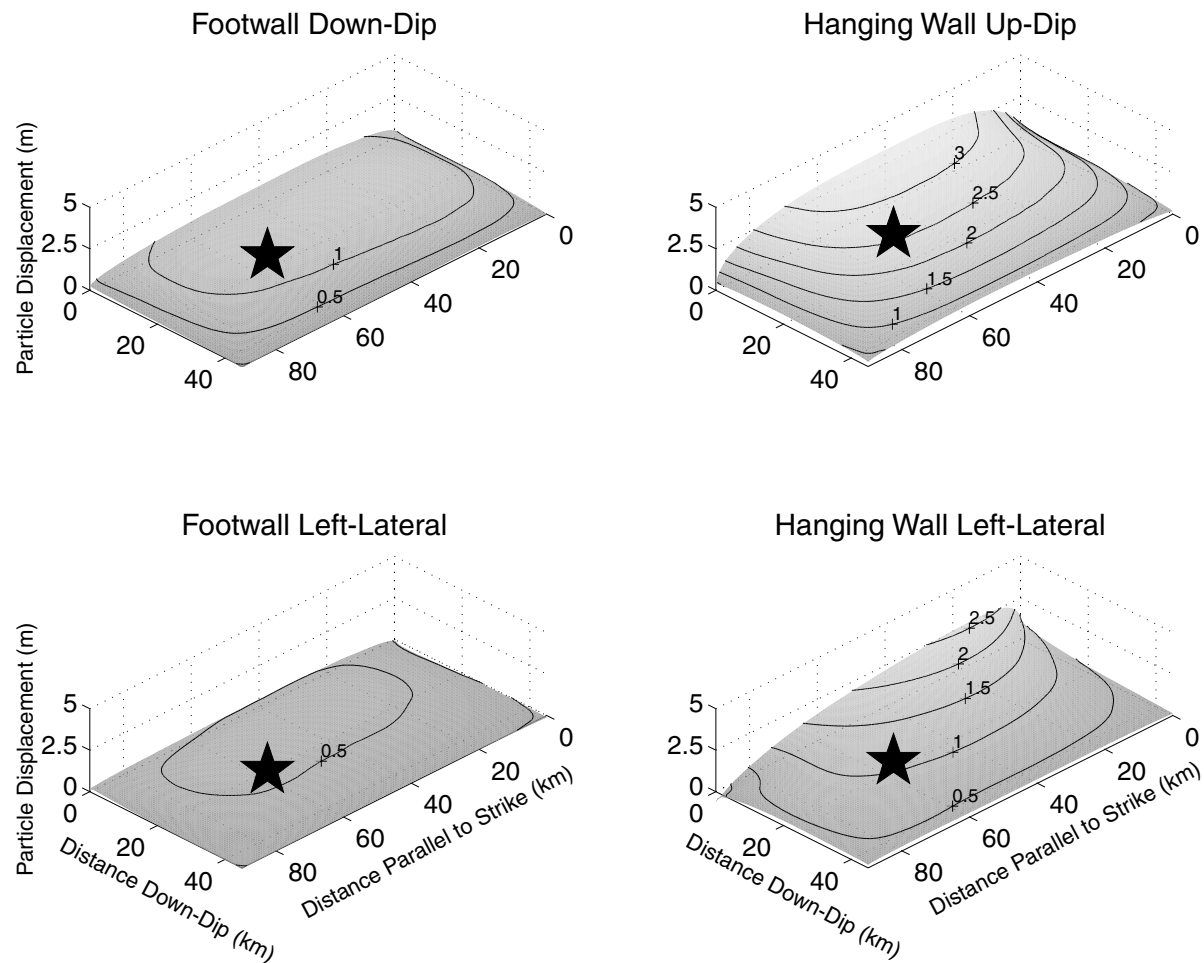


Figure 3. Fault displacements for the homogeneous prestress dynamic model. The star denotes the hypocenter, zero on the down-dip axis denotes the free surface, and zero on the strike-parallel axis denotes the northern edge of the fault. Note that the motion on the hanging wall is much greater than on the footwall and that the left-lateral component of motion increases to the north.

tirely consistent with the foam rubber models of Brune (1996), the static models of Rudniki and Wu (1995) and Bonafede and Neri (2000), and the dynamic models of Mikumo and Miyatake (1993), Oglesby *et al.* (1998), Shi *et al.* (1998), and Oglesby *et al.* (2000a,b). As in these studies, this asymmetry decreases with depth on the fault. Another clear feature of this model is the strong strike-slip component of motion, which has also been seen in three-dimensional static (Bonafede and Neri, 2000) and dynamic (Oglesby *et al.*, 2000b) models. An important aspect of this result is that the strike-slip motion is much larger in the hanging wall than in the footwall. The footwall has a strike-slip component that is approximately what one would expect from the rake of the shear prestress on the fault (67°). By contrast, the hanging wall has a highly variable strike-slip component that greatly increases in the north of the fault. The reason for the increased left-lateral strike-slip component in the north is that for a pure thrust fault, the hanging wall pushes outward

at each edge along strike. In the case of the Chi-Chi event, this would correspond to left-lateral motion in the north and right-lateral in the south. However, this motion is superimposed on an already slightly oblique (67°) rake. Thus, in the north of the fault, the outward motion of the hanging wall adds to the strike-slip motion, whereas in the south it subtracts from it. Another aspect of the fault motion is that the amplified strike-slip component is an even more surficial phenomenon than the overall hanging wall/footwall amplitude asymmetry. Bonafede and Neri (2000) attribute this effect to the higher deformation gradient in the hanging wall near the surface, leading to higher internal stresses and thus more motion in all directions in the hanging wall (a static effect). An additional effect, to be explored in more detail later, is the temporal nature of this change in rake away from the prestress direction. Some of this effect is due to traveling stress waves (Guatteri and Spudich, 1998; Spudich *et al.*, 1998), and contributes to the dynamic overshoot (Mada-

riaga, 1976) in the model. Additional issues concerning the dynamic overshoot in these models is discussed in more detail in the section on the static model.

The ground-motion manifestation of the fault motion in the homogeneous prestress case can be seen in the pattern of surface peak displacements. Figure 4 shows the horizontal components of peak displacement (i.e., the horizontal displacement vector having maximum amplitude) as a function of position. The peak displacements obtained from the doubly integrated acceleration records are shown on the left, and the peak displacements from the simulations are on the right. Even with essentially only the effects of fault dip (and no inhomogeneous stress or frictional properties on the fault), many of the features present in the Chi-Chi data can be seen in this model. In both the data and the model, there is a strong discontinuity between hanging-wall and footwall motion, with the hanging wall having much higher displacement than the footwall. Also, the strike-parallel component of hanging wall displacement in the north of the fault is quite obvious and leads to the remarkable observation that the hanging wall and the footwall are not moving in opposite directions (as might be assumed in a simple kinematic model). A similar comparison of the peak filtered horizontal velocity components between the data and homogeneous model is shown in Figure 5. The comparison is somewhat more difficult be-

cause velocity is a higher-frequency property and thus modeled less well by our method. Furthermore, velocity is more susceptible than displacement to unmodeled local site and propagation effects. Nonetheless, certain common features are present: in both the data and the model, there is a strong asymmetry between the hanging-wall and footwall peak velocities, and these velocities are much more strongly peaked near the fault trace.

Asperity Model

One feature in the data that is not reproduced well by the completely homogeneous stress field model is the larger relative amplitude in displacement and velocity in the north of the fault. Thus, our preferred model includes the asperity mentioned in the previous section. The fault displacements for this asperity model are shown in Oglesby and Day (2001) and are not reproduced here. However, it is worth mentioning again that the slip pattern is not radically different (aside from higher displacements in the asperity region) in general from the homogeneous model. In both cases, the hanging wall moves much more than the footwall, with this asymmetry decreasing with increasing depth on the fault. In addition, the hanging wall experiences much more strike-slip motion in the north of the fault than the footwall, but this motion is highly concentrated at the free surface.

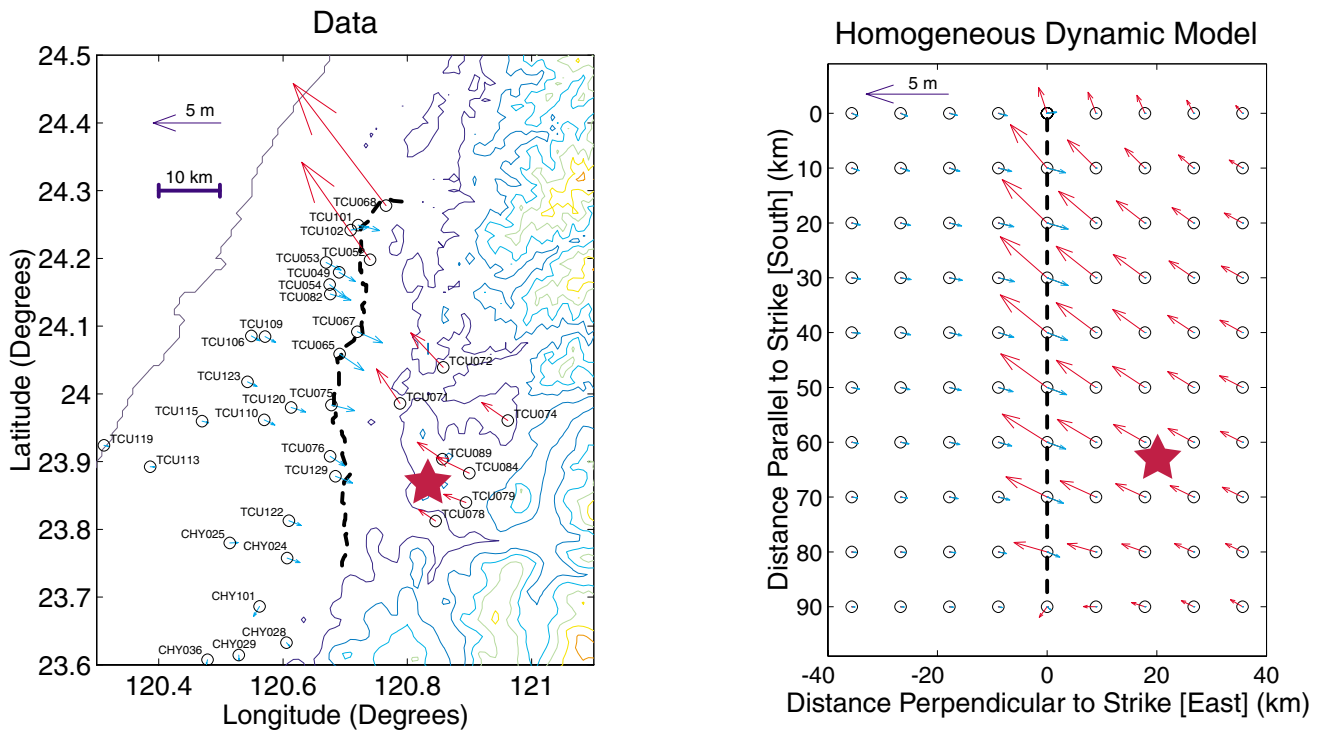


Figure 4. Comparison of peak horizontal surface displacements for the data (left) and the homogeneous dynamic model (right). Red corresponds to hanging-wall motion, and blue corresponds to the footwall motion. Note that both displacement distributions have higher motion on the hanging wall than on the footwall and a more left-lateral motion direction in the north of the fault. However, the relatively higher displacements in the north are not well modeled.

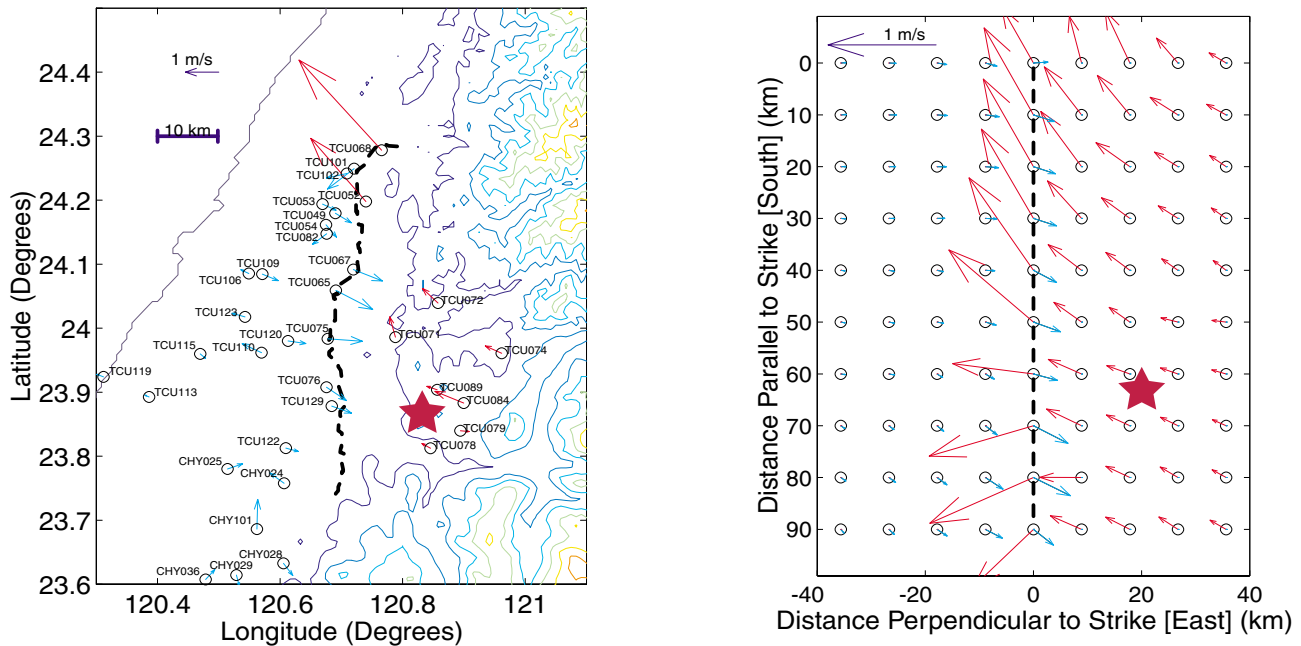


Figure 5. Comparison of peak horizontal velocities (filtered to 0.6 Hz) for the data (left) and the homogeneous dynamic model (right). Red corresponds to hanging-wall motion, and blue corresponds to the footwall motion. The peak velocities show features qualitatively quite similar to the peak displacements (Fig. 5) but are slightly less coherent. The peak velocities also show a much more pronounced peak right at the fault trace.

To compare with the results from our homogeneous model, in Figure 6 we reproduce (in a slightly modified form) from Oglesby and Day (2001) a comparison between the peak displacements in the data and our asperity model. Here again we see many of the common features of the homogeneous model, except in this case the displacements in the northern part of the modeled fault are much larger than in the southern part, providing a closer match to the pattern in the data. However, as in our homogeneous model, the peak model displacements (4.5 m) are still over a factor of 2 smaller than the peak data displacements (11 m). This discrepancy may be due to unmodeled site effects or complexities in the surficial part of the northern fault. Additionally, it is possible that a more finely tuned asperity in the north could eliminate this problem. However, it should be pointed out that while the absolute level of ground motion in the north depends on the location and size of the asperity, the qualitative pattern of peak displacements is rather insensitive to these properties—experiments with stronger asperities and asperities closer to the surface produced qualitatively similar distributions of peak ground displacement. Regardless of the quantitative underestimate in the north, the overall match in the ground-motion pattern is quite good, considering the simplicity of the model. Figure 7 compares the recorded and simulated peak velocities from our preferred dynamic model for the Chi-Chi event and also shows

most of the same features as the homogeneous model, except with a better match between the overall patterns of motion. Our even larger underprediction (by almost a factor of 4) of the peak velocities can largely be attributed to the homogeneous velocity structure used in our model, with no site or path amplification. This effect will be stronger for the peak velocities than for the peak displacements due to the higher-frequency nature of the velocity field.

As mentioned before, there is a temporal change in the direction of particle motion associated with the spatial pattern of dip-slip and strike-slip motion. Oglesby and Day (2001) show that in both the data and the model, the stations in the northern part of the fault initially start to move in the strike-slip (left-lateral) direction and then gradually start to rotate toward a more thrust-oriented direction. This temporal rake rotation between strike-slip and thrust motion is consistent with the work of Guatteri and Spudich (1998) and Spudich *et al.* (1998). These works showed that at the time of rupture, points on the fault are moving under the effects of the both static prestress and the dynamic stress waves that brought them to the point of failure. The stress waves (radiated by points elsewhere on the fault) are not necessarily in the same direction as the local static stress field, due to inhomogeneous prestress or simply to the radiation pattern. Thus, if the dynamic stresses are large with respect to the static stresses, then the initial movement direction of the

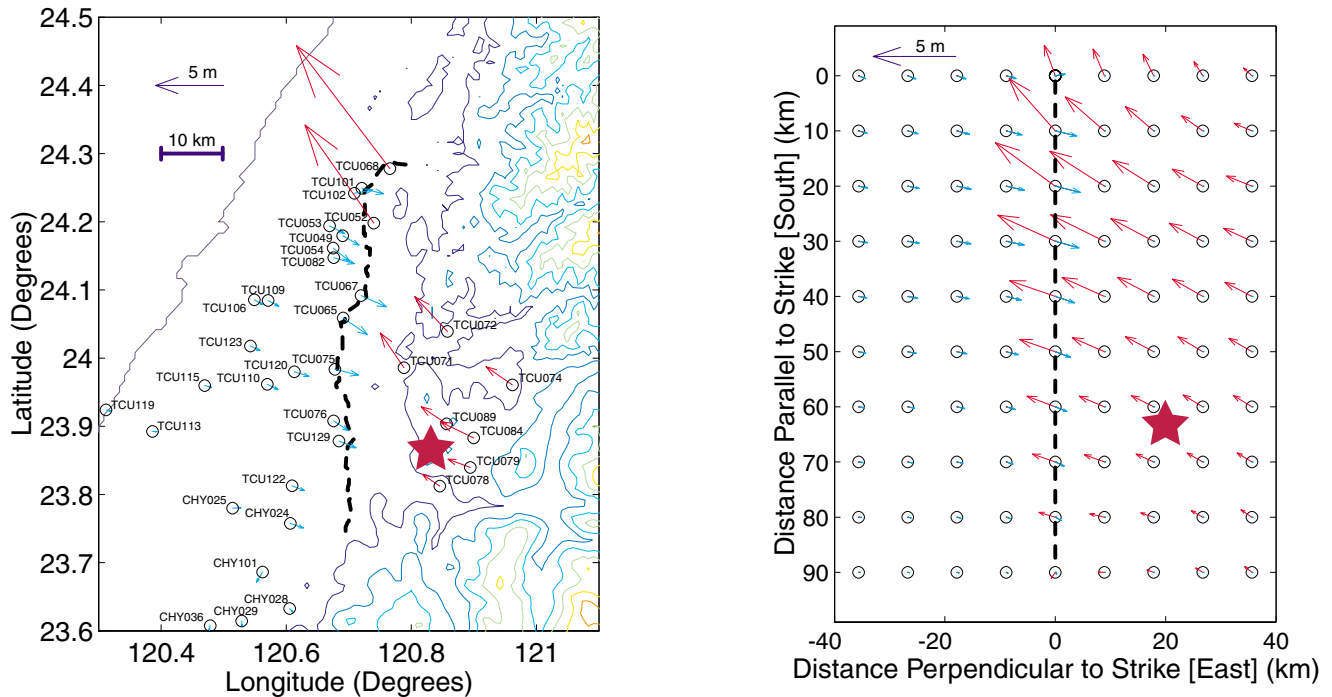


Figure 6. Comparison of peak horizontal surface displacements for the data (left) and the preferred asperity dynamic model (right). Red corresponds to hanging-wall motion, and blue corresponds to the footwall motion. As with the homogeneous model, both displacement distributions have higher motion on the hanging wall than on the footwall and a more left-lateral motion direction in the north of the fault. Additionally, the modeled peak displacements are larger in the north, in closer agreement with the data.

fault can be quite different from what would be implied by the static stresses. Of course, these effects will depend on the propagation of rupture on the fault and thus will be different for different hypocenter locations on the fault. Thus, it appears that the rake rotation pattern on the fault is due to a mixture of static and dynamic effects.

Static Asperity Model

The presence of a mixture of dynamic and static effects brings up an important question concerning dipping fault models: how many of the observed effects require a full dynamic simulation, and how many can be reproduced with a simpler static or dislocation model? To address this question we performed static simulations of the Chi-Chi earthquake using essentially the same method as the dynamic simulations, except (1) the frictional stress on the fault is set to be equal to the sliding frictional stress at all times over all the fault, and (2) the velocities are damped out to achieve faster convergence to the static solution. For computational expediency, in the static model we used a grid spacing with double the preferred grid spacing. However, extensive checking has shown that the current (static and dynamic) models are quite insensitive to grid spacing. The resulting final fault displacements are shown in Figure 8. The pattern of displacements is very similar to the preferred dynamic

model by Oglesby and Day (2001), but the amplitude is smaller overall. Despite the qualitative match between the dynamic and static displacements, the ratio of the dynamic and static displacements is a somewhat complicated distribution on the fault. The dynamic overshoot of the preferred dynamic model compared to the static model is most easily seen in Figure 9, which shows the ratio between the dynamic and static slips in the thrust and strike-slip components, as well as the ratio of total slip amplitudes. A few observations are clear. First, the average dynamic overshoot for this fault is approximately 70%, which is much higher than previously noted values between 15% and 35% (Madariaga, 1976; Archuleta and Frazier, 1978; Day, 1982). There are two likely reasons for this high overshoot. As argued previously, the dipping fault geometry amplifies the effects of dynamics. Simulations using the same fault prestress pattern but with a dip of 90° show a dynamic overshoot of less than 40% (much smaller, but still a rather high value). In addition, Madariaga (1976) has noted that higher rupture velocities lead to higher dynamic overshoots. Our rupture velocities approach the *S*-wave speed as they progress northward along the fault, which could further contribute to increased dynamic overshoot.

A second obvious feature of the distribution of dynamic overshoot on the fault is that in both the individual compo-

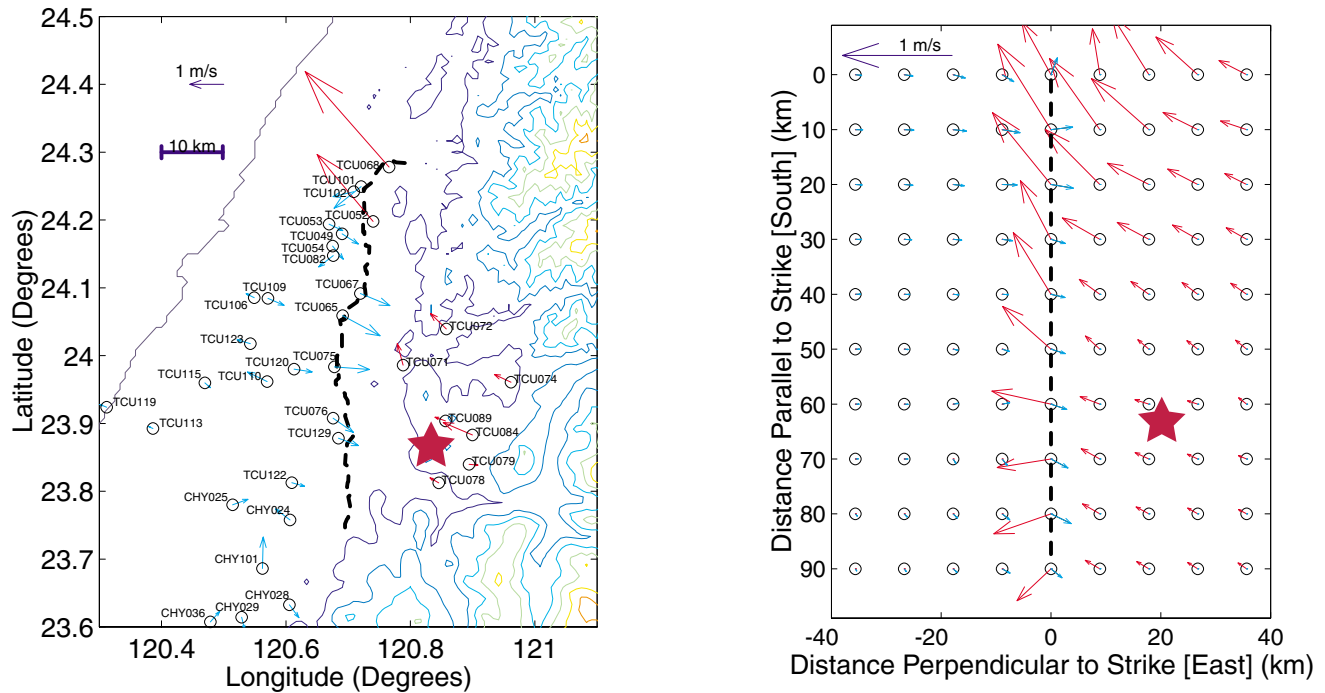


Figure 7. Comparison of peak horizontal velocities (filtered to 0.6 Hz) for the data (left) and the preferred asperity dynamic model (right). Red corresponds to hanging-wall motion, and blue corresponds to the footwall motion. As in the case of the peak displacements, the overall pattern of the simulation results is similar to the homogeneous model but shows better agreement with the increased motion in the north.

nents and in the total slip, the dynamic overshoot is small in the asperity but large in the lower-stress regions surrounding it. This effect is most likely due to the stress waves radiating from the asperity causing the less-stressed areas to slip more than they would have in the absence of the asperity. Even in a static calculation, the higher slip of a localized high stress region will leak out into the surrounding regions on the fault. However, stress waves will transmit this high-stress information much more effectively than the static stress field, and thus will cause greater slip in the surrounding region than would be obtained in a purely static model.

A final effect that can be seen in the ratios of dynamic to static slip is that the distributions of up-dip and strike-parallel overshoot are somewhat different, meaning that the direction of slip is slightly different between the dynamic and static cases. This effect is indicative of the dynamic contribution to rake rotation. The overall pattern of slip direction is dominated by static effects due to the fault geometry, but there is an additional dynamic contribution (due to the propagation of rupture) that can be seen in the final slips. Still, it is important to remember that the dynamic overshoot is in a sense the difference between performing a more rigorous (dynamic) model or a more simplified (static) model. The current results imply that for dipping faults, it is very important to consider dynamic effects. Regardless of the dynamic overshoot, a comparison between the final surface displacements for the dynamic asperity and static asperity

models (Fig. 10) shows very similar spatial patterns, including the hanging-wall/footwall asymmetry and increased strike-slip motion in the north. In spite of the quantitative differences between the static and dynamic solution, it would be difficult to choose which one qualitatively matches the pattern (excluding an overall scale factor) of near-source displacement better.

Discussion

An important implication of the current results is that certain aspects of fault and ground motion appear to be directly caused by the geometry of the fault—specifically, the dip angle between the fault plane and the free surface. This observation raises the possibility that certain ground motion features could be predicted before an earthquake occurs, if the fault geometry is well characterized ahead of time. In the absence of information about the state of stress or friction on the fault, the assumption of a homogeneous stress field (or a random stress field) is probably simplest. Thus, the current homogeneous model would constitute the fairest predictor for the behavior of the Chi-Chi fault prior to an earthquake on it. Using this model, the higher velocities and displacements in the north (which in our preferred model require a localized high-stress region) would not be predictable ahead of time. However, the greater motion on the hanging wall and the spatial variation of the rake direction

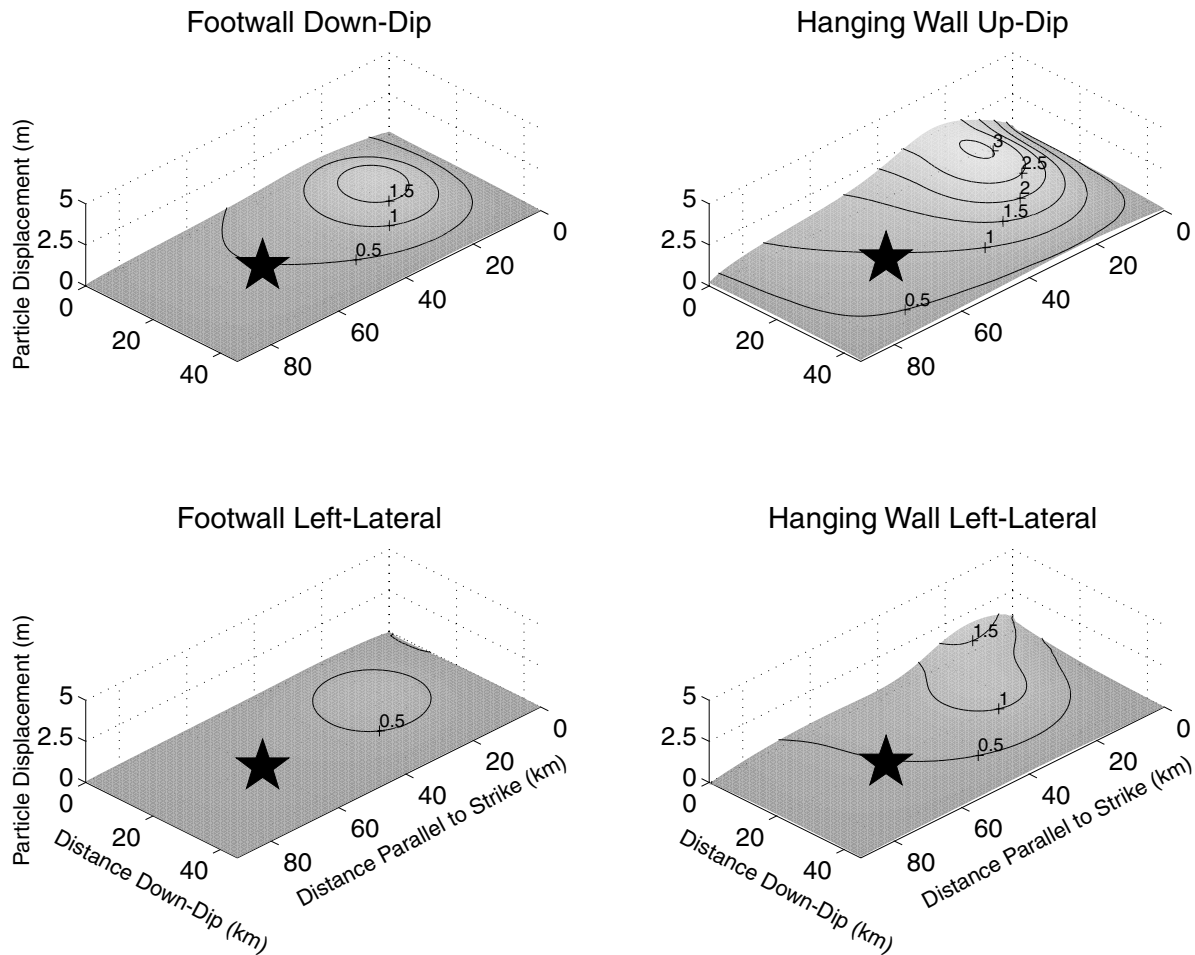


Figure 8. Fault displacements for the static model. The star denotes the hypocenter, zero on the down-dip axis denotes the free surface, and zero on the strike-parallel axis denotes the northern edge of the fault. The overall pattern of displacement is qualitatively similar to the preferred (asperity) dynamic fault displacements (Oglesby and Day, 2001), except the absolute value is significantly lower than the dynamic case.

could be predicted because these effects are due only to the fault geometry. The temporal rotation of rake is a more complicated effect due to a combination of the fault geometry and the dynamic effects of rupture propagation and radiation pattern. Thus, it is somewhat dependent on the unpredictable location of the hypocenter. Furthermore, a fault with high static stresses would likely respond less to the comparatively smaller effects of dynamic stresses (although near the free surface the static stresses should still be small). Regardless, some faulting features appear to be predictable, and even greater predictability could be achieved by using one's knowledge of the local material properties and site effects to better customize the earthquake model for the local region.

Even though the current work invokes fault geometry to explain a number of ground-motion observations, the planar fault geometry used in the models is clearly much simpler than the real Chi-Chi earthquake fault. The surface trace of the fault has many steps along strike, and it is likely that

there is even more nonplanar geometry at depth. However, Oglesby (1999) has shown that for thrust faults that intersect the surface, the spatial distribution of the near-source ground motion is dominated by the dip angle at the free surface. The deeper structure of the fault is much less important. Furthermore, the spatial patterns that this study fits are at a much larger scale than the variations of the fault geometry along strike. Thus, it is not surprising that such a simplified model is relatively successful in reproducing the near-source ground-motion pattern, especially on a large scale.

Conclusions

The main result of this work is that many of the observed features of the 1999 Chi-Chi earthquake can be explained through simple yet rigorous dynamic models that explicitly take into account the dipping fault geometry. These observations include higher motion on the hanging wall than on the footwall, high peak velocities concentrated

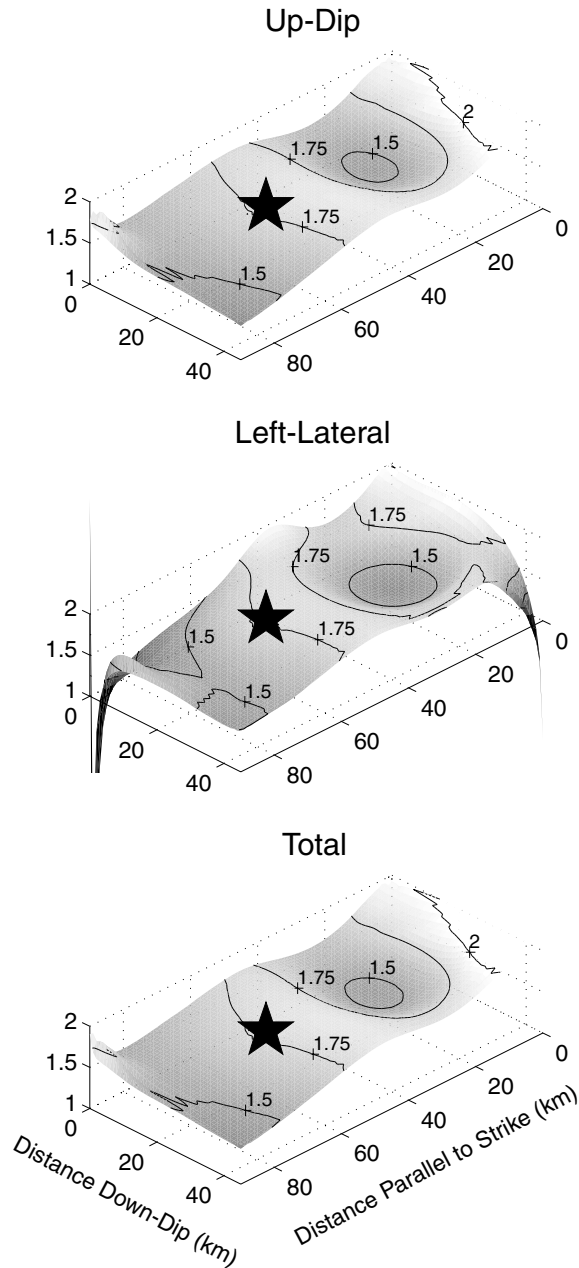


Figure 9. Distribution of dynamic overshoot (dynamic slip/static slip) in the up-dip and left-lateral directions as well as the ratio of total dynamic slip/total static slip. The star denotes the hypocenter, zero on the down-dip axis denotes the free surface, and zero on the strike-parallel axis denotes the northern edge of the fault. The dynamic overshoot is highly inhomogeneous on the fault and is larger than that of a vertical fault.

very near the fault trace on the hanging wall, and a change in the direction of rake from thrust to strike slip along the fault strike. These effects are shown to be due to the asymmetric dipping geometry of the fault. While an inhomogeneous stress distribution (an asperity model) provides a qual-

itatively somewhat better fit to the data, the aforementioned features of the Chi-Chi earthquake are present even in a purely homogeneous prestress model. The interpretation is that for thrust faults that intersect the surface of the earth, many features of the fault slip and near-source ground motion are dominated by the near-surface fault geometry and should be present for all faults of this type. A final result of the current models is that typical estimates of dynamic overshoot (15%–20%) may underpredict the dynamic overshoot for dipping faults because of amplified or additional dynamic effects not present in more symmetrical faulting situations. Dynamically caused temporal rake rotation further adds to the dynamic overshoot.

The current study does not attempt to model actual time histories and thus is not meant to replace more finely tuned models for this earthquake, which would produce waveforms or study the frictional properties on the fault. Additionally, it is important to note again that the current models do not attempt to match closely the absolute level of ground displacement or velocity—to do so would have required the inclusion of structural features that could have confused the interpretation of the effects of fault geometry. If one were predicting the ground motion in possible future earthquakes, clearly the three-dimensional earth structure and fault geometry would be required for accurate results. However, the current study does provide valuable guidance on what to look for in future faulting models. The geometrical effects can be thought of as an envelope for the overall particle motions, which on more precise scales are affected by all the aspects of faulting and wave propagation. The results also emphasize that in order to perform reliable dynamic earthquake models, fault geometry must be taken into account in a rigorous fashion, and that static models may seriously underpredict slip for faults with dipping geometry. In the future, it will be important to investigate the effects of other geometrical configurations, such as faults with multiple segments with different orientations. Armed with knowledge of the general effects of fault geometry, it may be possible to make relatively accurate predictions of at least some features of possible future earthquakes. This ability could have implications for seismic hazard estimation in earthquake-prone regions of the world.

Acknowledgments

The authors gratefully acknowledge the help and advice of Ralph Archuleta, Francis Wu, James Brune, and Alex Song. We also thank Yuehua Zeng and Chau-Huei Chen, who provided us with the GPS data. We finally thank the reviewers, who made many suggestions that greatly improved the quality of this manuscript. This work was supported by United States Geological Survey Grant 00HQGR0026, National Science Foundation grant EAR-9903099, and the Southern California Earthquake Center (SCEC). SCEC is funded by NSF Cooperative Agreement EAR-8920136 and USGS Cooperative Agreements 14-08-0001-A0899 and 1434-HQ-97AG01718. The SCEC Contribution Number for this article is 582.

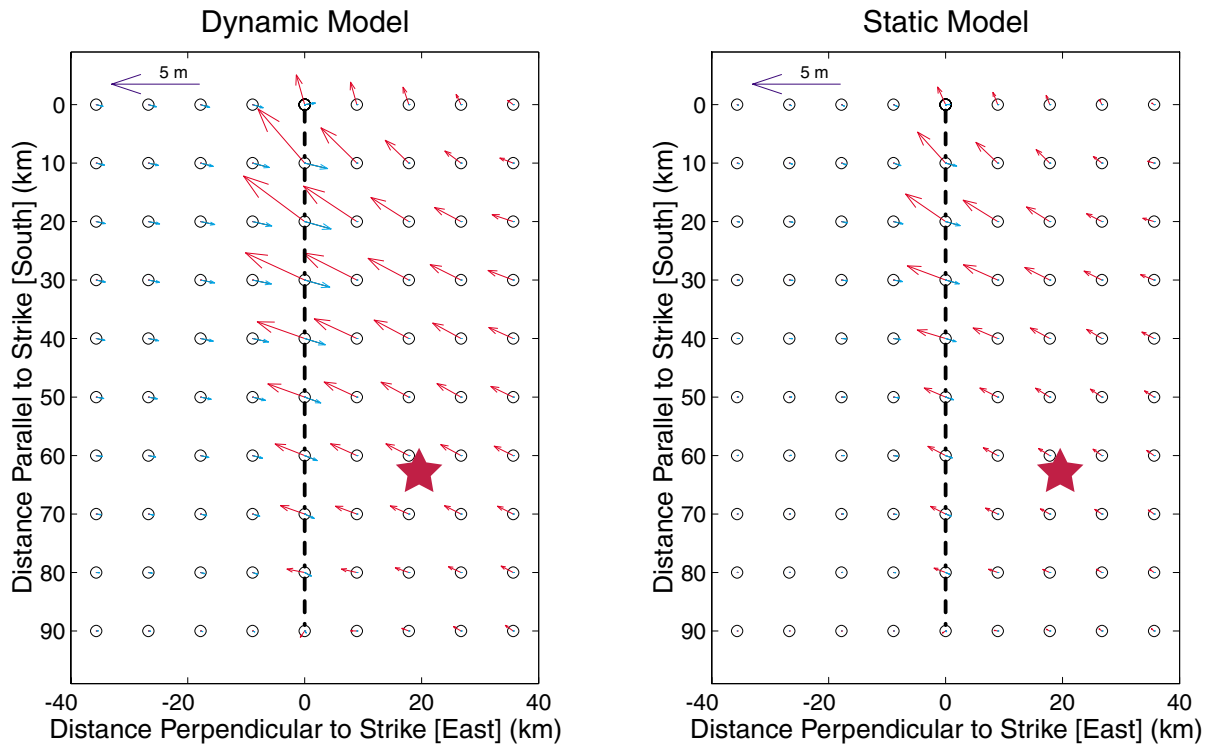


Figure 10. Comparison of the final surface displacement distributions for the dynamic (left) and static (right) models. Red corresponds to hanging wall motion, and blue to footwall motion. The dynamic displacements are significantly larger than the static case, but look qualitatively quite similar.

References

- Allen, C. R., J. N. Brune, L. S. Cluff, and A. G. Barrows (1998). Evidence for unusually strong near-field ground motion on the hanging wall of the San Fernando fault during the 1971 earthquake, *Seism. Res. Lett.* **69**, 524–531.
- Andrews, D. J. (1976). Rupture velocity of plane strain shear cracks, *J. Geophys. Res.* **81**, 5679–5687.
- Archuleta, R. J., and G. A. Frazier (1978). Three-dimensional numerical simulations of dynamic faulting in a half-space, *Bull. Seism. Soc. Am.* **68**, 541–572.
- Bonafede, M., and A. Neri (2000). Effects induced by an earthquake on its fault plane: a boundary element study, *Geophys. J. Int.* **141**, 43–56.
- Boore, D. M. (1999). Effect of baseline corrections on response spectra for two recordings of the 1999 Chi-Chi, Taiwan, earthquake, *U.S. Geol. Surv. Open-File Rept.* 99-545.
- Brune, J. (1996). Particle motions in a physical model of shallow angle thrust faulting, in *Proc. Indian Acad. Sci. (Earth Planet. Sci.)* **105**, L197–L206.
- Chin, T. C., K. W. Kou, W. H. K. Lee, T. L. Teng, and Y. B. Tsai (2000). A preliminary report on the 1999 Chi-Chi (Taiwan) earthquake, *Seism. Res. Lett.* **71**, 24–30.
- Day, S. M. (1982). Three-dimensional simulation of spontaneous rupture: the effect of nonuniform prestress, *Bull. Seism. Soc. Am.* **72**, 1881–1902.
- Guatterri, M., and P. Spudich (1998). Coseismic temporal changes of slip direction: the effect of absolute stress on dynamic rupture, *Bull. Seism. Soc. Am.* **88**, 777–789.
- Harris, R. A., and S. M. Day (1993). Dynamics of fault interaction: parallel strike-slip faults, *J. Geophys. Res.* **98**, 4461–4472.
- Harris, R. A., and S. M. Day (1999). Dynamic 3D simulations of earthquakes on en echelon faults, *Geophys. Res. Lett.* **26**, 2089–2092.
- Harris, R. A., R. J. Archuleta, and S. M. Day (1991). Fault steps and the dynamic rupture process: 2-D numerical simulations of a spontaneously propagating shear fracture, *Geophys. Res. Lett.* **18**, 893–896.
- Ida, Y. (1972). Cohesive force across the tip of a longitudinal-shear crack and Griffith's specific surface energy, *J. Geophys. Res.* **77**, 3796–3805.
- Iwan, W. D., M. A. Moser, and C.-Y. Peng (1985). Some observations on strong-motion earthquake measurement using a digital accelerograph, *Bull. Seism. Soc. Am.* **75**, 1225–1246.
- Kase, Y., and K. Kuge (1998). Numerical simulation of spontaneous rupture process on two non-coplanar faults: the effect of geometry on fault interaction, *Geophys. J. Int.* **135**, 911–922.
- Lee, W. H. K., T. C. Shin, K. W. Kuo, and K. C. Chen (1999). CWB free-field strong-motion data from the 921 Chi-Chi earthquake, digital acceleration files on CD-ROM, prepublication version (December 6, 1999), Seismology Center, Central Weather Bureau, Taipei, Taiwan, Vol. 1.
- Madariaga, R. (1976). Dynamics of an expanding circular fault, *Bull. Seism. Soc. Am.* **66**, 639–666.
- Magistrale, H., and S. M. Day (1999). Simulations of multi-segment thrust fault rupture, *Geophys. Res. Lett.* **26**, 2093–2096.
- Mikumo, T., and T. Miyatake (1993). Dynamic rupture process on a dipping fault, and estimates of stress drop and strength excess from the results of waveform inversion, *Geophys. J. Int.* **112**, 481–496.
- Mori, J. J., and K.-F. Ma (2000). Slip velocity estimates of the 1999 Chi-Chi, Taiwan, earthquake: new observations of fault dynamics, *EOS Trans. Am. Geophys. Union* **81**, 140–141.
- Ni, S., J. N. Brune, G. Choy, J. G. Anderson, and Y. Zeng (1999). Local and teleseismic estimates of radiated energy and apparent stress from the Chi-Chi, Taiwan earthquake: evidence for inertial detachment of the hanging wall from the footwall in thrust faulting, in *AGU 1999 Fall Meeting Program*, 13–17 December, San Francisco, 13.

- Nielsen, S. B. (1998). Free surface effects on the propagation of dynamic rupture, *Geophys. Res. Lett.* **25**, 125–128.
- Oglesby, D. D. (1999). Earthquake Dynamics on Dip-Slip Faults, *Ph.D. Thesis*, University of California, Santa Barbara.
- Oglesby, D. D., and S. M. Day (2001). The effect of fault geometry on the 1999 Chi-Chi (Taiwan) earthquake, *Geophys. Res. Lett.* **28**, 1831–1834.
- Oglesby, D. D., R. J. Archuleta and S. B. Nielsen (1998). Earthquakes on dipping faults: the effects of broken symmetry, *Science* **280**, 1055–1059.
- Oglesby, D. D., R. J. Archuleta, and S. B. Nielsen (2000a). Dynamics of dip-slip faulting: explorations in two dimensions, *J. Geophys. Res.* **105**, 13,643–13,653.
- Oglesby, D. D., R. J. Archuleta, and S. B. Nielsen (2000b). The three-dimensional dynamics of dipping faults, *Bull. Seism. Soc. Am.* **90**, 616–628.
- Rau, R., J. Yu, T. Yu, M. Yang, and C. Tseng (1999). Co-seismic displacements of the 1999 Chi-Chi, Taiwan, earthquake sequence, in *AGU 1999 Fall Meeting Program*, 13–17 December, San Francisco.
- Rudniki, J., and M. Wu (1995). Mechanics of dip-slip faulting in an elastic half-space, *J. Geophys. Res.* **100**, 22,173–22,186.
- Shi, B., A. Anooshehpour, J. N. Brune, and Y. Zeng (1998). Dynamics of thrust faulting: 2D lattice model, *Bull. Seism. Soc. Am.* **88**, 1484–1494.
- Shin, T. L., F. T. Wu, J. K. Chung, R. Y. Chen, Y. M. Wu, C. S. Chang, and T. L. Teng (2001). Ground displacements around the fault of the September 20, 1999, Chi-Chi, Taiwan, earthquake, *Geophys. Res. Lett.* **28**, 1651–1654.
- Song, T.-R. A. (2000). New theoretical relations of ground acceleration, slip velocity and rupture velocity, and their implications, *EOS Trans. Am. Geophys. Union* **81**, 141.
- Spudich, P., M. Guatteri, K. Otsuki, and J. Minagawa (1998). Use of fault striations and dislocation models to infer tectonic shear stress during the 1995 Hyogoken Nanbu (Kobe) earthquake, *Bull. Seism. Soc. Am.* **88**, 413–427.
- Teng, T. L. (2000). Jumping Dislocations: the 1999 Chi-Chi, Taiwan earthquake, *Seism. Res. Lett.* **71**, 205.
- Whirley, R. G., and B. E. Engelmann (1993). *DYNA3D: A Nonlinear, Explicit, Three-Dimensional Finite Element Code for Solid and Structural Mechanics: User Manual*, University of California, Lawrence Livermore National Laboratory, Livermore, California, UCRL-MA-1107254 Rev. 1.
- Zeng, Y., and C. Chen (2001). Fault rupture process of the 20 September 1999 Chi Chi, Taiwan, earthquake, *Bull. Seism. Soc. Am.* **91**, no. 5, 1088–1098.

Department of Geological Sciences
 San Diego State University
 5500 Campanile Ave
 San Diego, California 92182-1020
 doglesby@moho.sdsu.edu
 clay@moho.sdsu.edu

Manuscript received 31 July 2000.